The Astrophysical Journal Letters, 897:L23 (7pp), 2020 July 10 https://doi.org/10.3847/2041-8213/ab9d7a

Differences in Periodic Magnetic Helicity Injection Behavior between Flaring and Non-flaring Active Regions: Case Study

M. B. Korsós[1,2], P. Romano[3], H. Morgan[1], Y. Ye[4], R. Erdélyi[2,5], and F. Zuccarello[6]
[1] Department of Physics, Aberystwyth University, Ceredigion, Cymru SY23 3BZ, UK
[2] Department of Astronomy, Eötvös Loránd University, Pázmány Péter sétány 1/A, H-1112 Budapest, Hungary
[3] INAF Osservatorio Astrofisico di Catania, Via S. Sofia 78, I-95123 Catania, Italy
[4] Space Science Institute, Macau University of Science and Technology, Macao, People's Republic of China
[5] Solar Physics & Space Plasma Research Center (SP2RC), School of Mathematics and Statistics, University of Sheffield, Hounsfield Road S3 7RH, UK
[6] Dipartimento di Fisica e Astronomia "Ettore Majorana," Università di Catania, Via S. Sofia 78, I-95123 Catania, Italy
Received 2020 May 8; revised 2020 June 10; accepted 2020 June 13; published 2020 July 8

Abstract

The evolution of magnetic helicity has a close relationship with solar eruptions and is of interest as a predictive diagnostic. In this case study, we analyze the evolution of the normalized emergence, shearing, and total magnetic helicity components in the case of three flaring and three non-flaring active regions (ARs) using Spaceweather Helioseismic Magnetic Imager Active Region Patches vector magnetic field data. The evolution of the three magnetic helicity components is analyzed with wavelet transforms, revealing significant common periodicities of the normalized emergence, shearing, and total helicity fluxes before flares in the flaring ARs. The three non-flaring ARs do not show such common periodic behavior. This case study suggests that the presence of significant periodicities in the power spectrum of magnetic helicity components could serve as a valuable precursor for flares.

Unified Astronomy Thesaurus concepts: Solar flares (1496); Solar activity (1475); Solar active region magnetic fields (1975); Sunspots (1653); Solar active regions (1974); Space weather (2037)

1. Introduction

Space weather refers to the short-term interaction of different manifestations of solar activity with geospace that occurs through a complex series of dynamic events. These interactions can result in hazardous conditions for the functioning of many vital socioeconomic infrastructures, both terrestrial (e.g., long-distance oil/gas pipelines, electric power grids, aviation-control, high-frequency (HF) radio communication) and space-based (e.g., communication satellites, global positioning systems, ISS), leading to a reduced or total lost capacity (Eastwood et al. 2017, and references therein). Advancements of solar eruption forecasting capabilities through the identification of observable precursors at the Sun is crucial (see, e.g., Barnes et al. 2016; Leka et al. 2019, and references therein). This forecasting is challenging, in particular understanding the physical processes that underpin solar eruptions (see, e.g., Florios et al. 2018; Campi et al. 2019; Korsós et al. 2019; Wang et al. 2019).

Flares and coronal mass ejections (CMEs) originate mostly from magnetically complex, highly twisted, and sheared elements of a δ-type active region (AR; e.g., Georgoulis et al. 2019; Toriumi & Wang 2019, and references therein). The evolution of the magnetic helicity (Elsasser 1956) is likely to be a key physical process that precedes flare and/or CME events, and measurements of helicity derived from photospheric magnetic field data can provide insight into the underlying mechanism(s) of these events. Many observational studies have found a relationship between the temporal evolution of helicity flux and flares/CMEs.

Moon et al. (2002a, 2002b) found that a significant amount of helicity is injected before large flare events. Smyrli et al. (2010) investigated the helicity flux in a case study of 10 ARs and reported a sudden change in the helicity flux was present during six flares. Park et al. (2008, 2012) discovered that the helicity flux slowly increases and then remains constant just before flares. Park et al. also reported that the injected helicity flux changed its sign before some very impulsive flare and CMEs. Tziotziou et al. (2013) studied the dynamic evolution of AR 11158 before flares and CMEs, and found that eruption-related decreases, and subsequent free-energy and helicity budgets, were consistent with the observed eruption magnitude. Other works addressed also that the helicity flux reversed sign around at the start of a flare (Vemareddy et al. 2012; Wang et al. 2014; Gao 2018), caused by the interaction between the associated magnetic flux tubes with opposite signs of helicity (Linton et al. 2001; Kusano et al. 2004; Liu et al. 2007; Chandra et al. 2010; Romano et al. 2011; Romano & Zuccarello 2011). It is suggested that a CME can also remove helicity from its source, leading to a lower total AR potential magnetic energy (Démoulin et al. 2002; Smyrli et al. 2010). On the other hand, based on numerical data, Pariat et al. (2017) claimed that magnetic energies and the total relative helicity are not effective diagnostics for flare prediction, but the decomposition of the relative magnetic helicity introduced by Berger (2003), in the current-carrying component and its counterpart, may be useful. Based on solar magnetic field observations, Thalmann et al. (2019) gave similar conclusions to Pariat et al. (2017). They reported that the ratio of current-carrying to total helicity is capable of indicating an eruptive AR, but not the magnitude of an upcoming eruption.

To the best of our knowledge, no previous studies have found a relationship between the oscillatory behavior of the evolution of magnetic helicity (or its various components) and flaring activities that may be related to such oscillations. A recent theoretical study by Prior et al. (2020) reported that the multi-resolution wavelet decomposition is useful to analyze the spatial scales of helicity in magnetic fields in a manner that is consistently additive. To investigate distinctive behavior patterns of helicity flux in flaring and non-flaring ARs as a case study to demonstrate the concept, we focus here on the

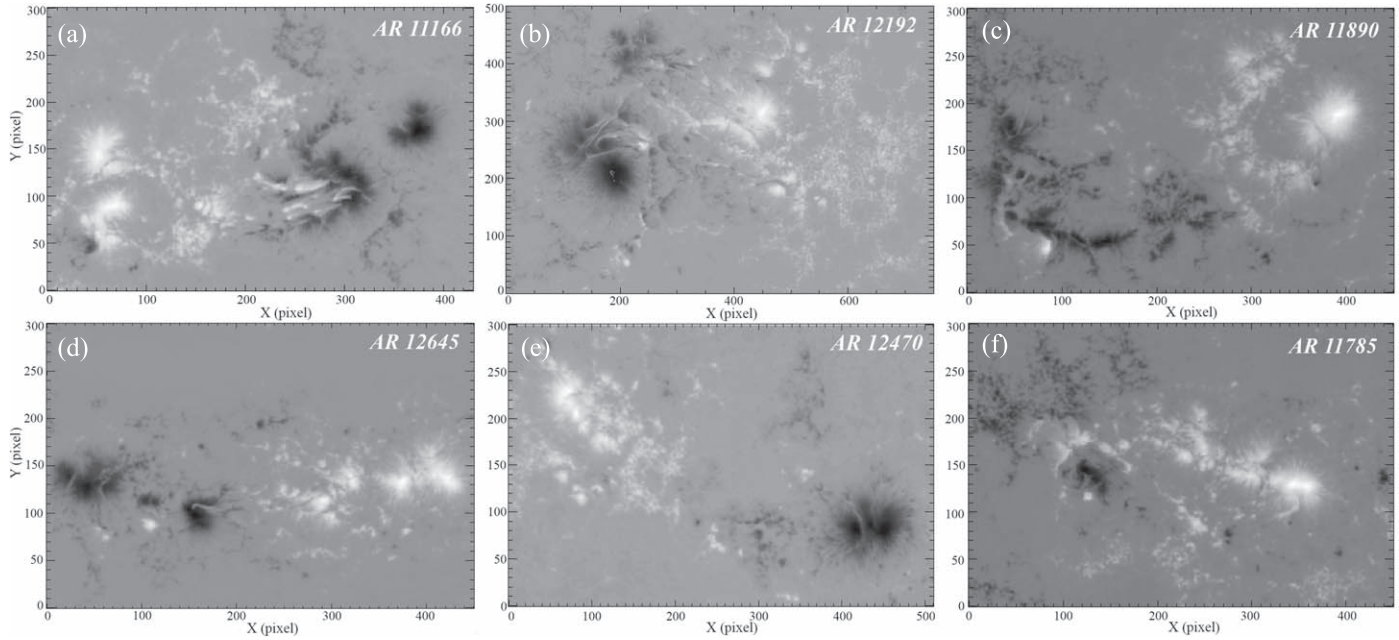

Figure 1. Six panels showing the radial component of magnetic field in (a) AR 11166 on 2011.03.10 20:24:00, (b) AR 12192 on 2014.10.24 00:00:00, (c) AR 11890 on 2013.11.08 00:00:00, (d) AR 12645 on 2017.04.02 00:00:00, (e) AR 12470 on 2015.12.17 00:00:00, and (f) AR 11785 on 2013.07.09 00:00:00. The *x*- and *y*-axes are expressed in pixels, where one pixel is related to the $0\farcs5$ resolution of SDO/HMI.

evolution of the magnetic helicity injection rate through wavelet analyses during the observable disk passage period of six ARs.

The work is structured as follows. Section 2 describes the adopted tools for the helicity flux calculations and the selection criteria of these six investigated ARs. In Section 3, we describe the analysis and present the results. Key findings and conclusions, along with a suggestion of future work, are given in Section 4.

2. Magnetic Helicity Flux Calculation

The magnetic helicity is a proxy for the 3D complexity of a magnetic field in a volume; thus, it is often interpreted as a generalization of more local properties such as magnetic twist and shear. Taylor (1974) and Woltjer (1958) introduced the concept of magnetic helicity as a well-conserved quantity, even in non-ideal magnetohydrodynamics. Berger & Field (1984) proved that helicity is conserved in conductive plasma, meaning that helicity variations with respect to time are essentially restricted to helicity flow through a surface S. Berger & Field (1984) showed that magnetic helicity dissipates very slowly during the course of magnetic reconnection.

To monitor the helicity flux (i.e., the helicity injection rate) through the photosphere over an AR, we use the following equation:

$$\left.\frac{dH}{dt}\right|_S = 2\int_S (\boldsymbol{A}_p \cdot \boldsymbol{B}_h)\boldsymbol{v}_{\perp z}\,dS - 2\int_S (\boldsymbol{A}_p \cdot \boldsymbol{v}_{\perp h})\boldsymbol{B}_z\,dS, \quad (1)$$

introduced by Berger (1984). $\boldsymbol{A}_p$ is the vector potential of the potential magnetic field $\boldsymbol{B}_\mathrm{p}$. $\boldsymbol{B}_h$ and $\boldsymbol{B}_z$ denote the tangential and normal components of the magnetic field vector with respect to the surface S, and $\boldsymbol{v}_{\perp h}$ and $\boldsymbol{v}_{\perp z}$ are the tangential and normal components of velocity. The first term on the right side arises from twisted magnetic flux tubes emerging from the solar interior into the corona (hereafter the emergence term), while the second term is generated by the shearing and braiding of the field lines by tangential motions on the solar surface (hereafter the shearing term). $\boldsymbol{A}_p$ is determined by the photospheric magnetic field and the Coulomb gauge (Berger 1997; Berger & Ruzmaikin 2000).

For magnetic helicity calculation, reliable and continuous photospheric vector magnetograms are required in order to determine the associated photospheric velocity fields. Therefore, we use *hmi.sharp_cea_720s* vector magnetic field measurements of the Spaceweather Helioseismic Magnetic Imager Active Region Patches (SHARPs[7]), with a 12 minute cadence (Bobra et al. 2014). The photospheric plasma velocity is calculated by applying the Differential Affine Velocity Estimator for Vector Magnetograms (DAVE4VM[8]) algorithm (Schuck 2008). The window size used in the calculations is 19 pixels, which was determined by examining the non-parametric Spearman rank order correlation coefficients, Pearson correlation coefficients and slopes between $\Delta_h \cdot (v_z \boldsymbol{B}_h - \boldsymbol{v}_h \boldsymbol{B}_z)$ and $\delta \boldsymbol{B}_z / \delta t$ (Schuck 2008). The vector potential $\boldsymbol{A}_p$ is derived using MUDPACK (for details see, e.g., Adams 1993), a multigrid software for solving elliptic partial differential equations.

In this case study, we analyze the magnetic helicity flux evolution of six ARs, namely NOAA ARs 11166, 11785, 11890, 12192, 12470, and 12645 (see Figure 1), which were selected to satisfy the following criteria.

1. The selected ARs respect the Hale–Nicholson law (Hale & Nicholson 1925) of solar cycle 24. Some works claim that AR that violate the Hale–Nicholson law are more flare/CME productive (Elmhamdi et al. 2014, and references therein).
2. The ARs have a prevalent bipolar configuration.
3. The ARs have δ-spot(s).

[7] http://jsoc.stanford.edu/doc/data/hmi/sharp/sharp.htm
[8] https://ccmc.gsfc.nasa.gov/lwsrepository/DAVE4VM_description.php

Table 1
Summary Table of the Properties of the Studied Six ARs: NOAA Number and the Study Period of AR, Information about the Investigated Flares, Dominant Evolution Phase of the ARs

AR	Flare Class	Flare Time	Evolutionary Phase	δ-spot
		Flaring ARs		
AR 11166	X1.5	2011 Mar 9 23:23	Emergence	2011 Mar 5–11
2011 Mar 4–11				
AR 12192	X1.1	2014 Oct 19 05:03	Stable	2014 Oct 19–27
2014 Oct 19–27	M8.7	2014 Oct 22 01:59		
	X1.6	2014 Oct 22 14:28		
	X3.1	2014 Oct 24 21:41		
	X1.0	2014 Oct 25 17:08		
	X2.0	2014 Oct 26 10:56		
AR 11890	X3.3	2013 Nov 5 22:12	Decay	2013 Nov 4–12
2013 Nov 4–12	X1.1	2013 Nov 8 04:26		
	X1.1	2013 Nov 10 05:14		
		Non-flaring ARs		
AR 12645	B/C		Emergence	2017 Apr 2–6
2017 Mar 29–Apr 7				
AR 12470	B/C		Stable	2015 Dec 15–16
2015 Dec 15–22				
AR 11785	B/C		Decay	2013 Jul 4–8
2013 Jul 4–12				

Note. The last coulomb shows the time interval when δ-spot(s) appeared in an AR.

4. The ARs have two distinct behaviors in terms of flare activity. ARs 11166, 11890, and 12192 were host of intense M- and X-class flares, and are grouped as "flaring." ARs 11785, 12470, and 12645 only produced B- and C-class flares and are grouped as "non-flaring."
5. The AR is not a cradle of significant/fast CME eruptions that have linear velocities larger than $\sim$1000 km s^{-1}. In this regard, ARs 11166 and 11890 produced slow CMEs only, with 400–700 km s^{-1} linear speeds. AR 12192 was rich in terms of flaring but not in term of CMEs.
6. In each of the flaring/non-flaring groups, one AR is characterized to be dominantly either in formation (ARs 11166 and 12645), or fully developed (ARs 12192 and 12470), or in a decaying (ARs 11890 and 11785) evolutionary phase during the investigated period.

Table 1 summarizes the time interval of observations of the six ARs. Each time interval is limited to a duration when the corresponding AR is between $-60°$ and $+60°$ with respect to the central meridian to avoid extreme magnetic field projection effects (Bobra et al. 2014). Table 1 includes also the onset time and the associated GOES class of the flares occurred in each AR, based on the GOES solar flare catalog.[9] Furthermore, Table 1 gives information on the dominant evolutionary phases of the ARs, and on how long their δ-spots were observed.

3. Data Analysis

The emergence and shearing components of the magnetic helicity of the six ARs are calculated using Equation (1). The total magnetic helicity flux for a given AR was generated by summing the emergence and shearing components. The three helicity injection rates for each AR were obtained by integrating the helicity flux over the entire area of the AR. The three helicity flux components are further normalized by their respective largest absolute value in order to facilitate comparison on similar scales. The normalized emergence, shearing, and total helicity fluxes are shown in the top panels of Figures 2–3. In the upper panels of Figures 2–3, the blue line is the emergence term, the red line the magnetic helicity flux associated with shearing motions at the photosphere, and the black line is the total magnetic flux.

By inspecting the top panels of Figures 2–3(a)–(c), we can see that the normalized shearing and total helicity flux components show similar evolution trends in each of the six AR cases, which suggests that the shearing motion plays a more important role in the evolution of total helicity. The emergence helicity flux develops differently when compared to the two other components, see, e.g., in case of AR 11890 or 12470. Furthermore, we can also identify various quasi-periodic patterns in the evolution of the three helicity components, for both flaring and non-flaring AR cases. However, to reveal a possible diacritical periodic signal(s) between the two groups, we construct wavelet power spectra (WPS) using a software developed by Torrence & Compo (1998), employing the default Morlet wavelet profile. The associated global power spectrum (GPS) is also calculated as the WPS averaged over time for each case. This is similar to a Fourier power spectrum. The significance level of the WPS, at 1σ confidence level, is estimated using a white noise model and the standard deviation of the input signal. This significance is a function of the periodicity. Therefore, the ratio of the WPS to the significance level is useful to identify significant

[9] https://hesperia.gsfc.nasa.gov/

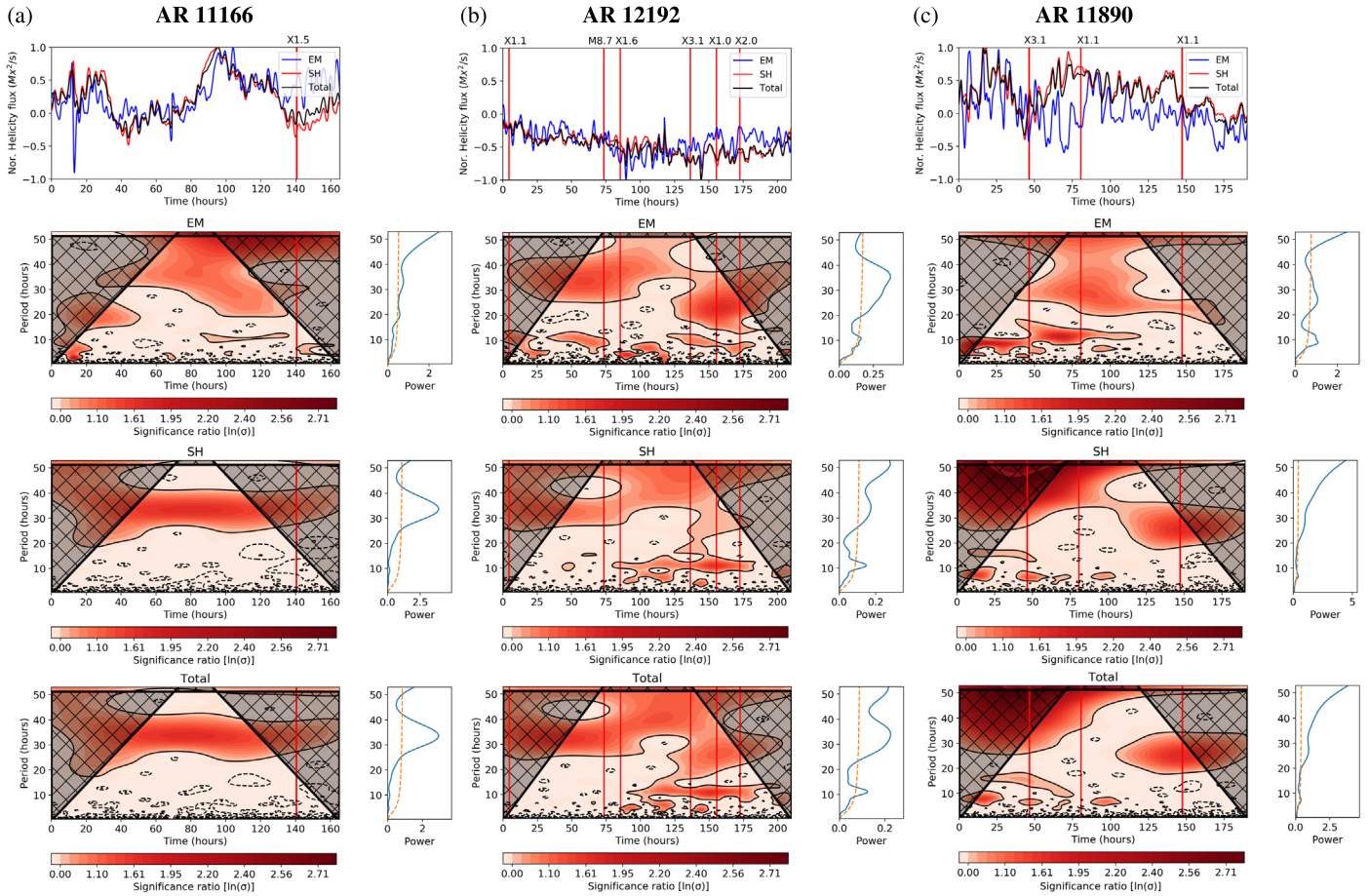

Figure 2. Time analysis of three flaring ARs, namely (a) AR 11166 (b) AR 12192, and (c) AR 11890. The top panels show time series of the normalized emergence (EM, blue), shearing (SH, red), and total (Total, black) helicity fluxes. The red vertical lines mark the onset time of flares. The second through fourth rows show the wavelet power spectrum (WPS) of the normalized emergence, shearing, and total helicity fluxes, respectively. Rather than plotting power directly, the color bars visualize the logarithm of the ratio of the power to the expected power for Gaussian-distributed white noise and significance compared to noise. The x-axis of each WPS is the observation time, and the y-axis is the period, both in hours. On the WPS plots, the black lines bound the cone-of-influence, i.e., the domain where edge effects become important. The plots to the right of each WPS are the corresponding global wavelet spectra (power averaged over time, similar to a Fourier power spectrum). The orange dashed lines mark the one σ confidence in global wavelet spectrum analyses.

periodicities—we call this value the significance ratio. In Figures 2–3(a)–(c), the natural logarithm of this ratio is displayed, therefore values of 0 or higher (or within the black contours) are significant.

In Figures 2–3(a)–(c), the WPS and GPS of the emergence (EM), shearing (SH) and total (Total) helicity fluxes are shown, after application of a high-pass filter. The original data series is smoothed with a timescale of two-thirds of the full length of the time series, and the resulting smoothed series is subtracted from the original data series, thus damping power at long periods. This is an important step because slow changes that are not of immediate interest for this study may affect the calculation of significance levels at shorter periods (McAteer et al. 2002). In this study, a significant period is identified as (i) a significance ratio larger than 1 (i.e., that is 0 on the ln scale) measured in σ, and (ii) the peak in the GPS is above the confidence level (shown as the dashed orange line in the GPS plots).

Based on Figures 2(a)–(c), in the case of three flaring ARs, there are common peak(s) of the EM, SH, and total helicity flux components in the WPS and GPS preceding the flare occurrences. In particular:

1. AR 11166: in Figure 2(a), a powerful the 34 hr periodicity is present in the GPS of the EM, SH, and total helicity fluxes about 5 days prior to the X1.5 flare occurrence. The WPS shows that 34 hr periodicity persists for a lifetime of ∼three cycles in the EM time series and declines after the flare. However, this periodicity continues to play an important role for five cycles in the SH and total helicity fluxes. The EM shows a 20 hr short-lived periodicity (two cycles) near the start of the time series. This feature is a result of the abrupt large negative value in EM that is not present in the data of SH and in the total flux components. It is interesting to note that the 20 hr periodicity coincides with the large variations (and even a change in sign) in the EM, and could be related to the findings of Smyrli et al. (2010) and/or Park et al. (2008, 2012) mentioned in the Introduction.
2. AR 12192: there are two common peaks in periodicities in the three helicity flux components; see Figure 2(b). First, a ∼35 hr strong periodicity is observable before the M8.6 and X1.6 flares in the EM, SH, and total flux time series, as shown in both the WPS and GPS. After the M8.6 and X1.6 flares, a ∼10 hr periodicity also becomes dominant next to the ∼35 hr prior to the remaining three X-class flares. This ∼10 hr common periodicity is

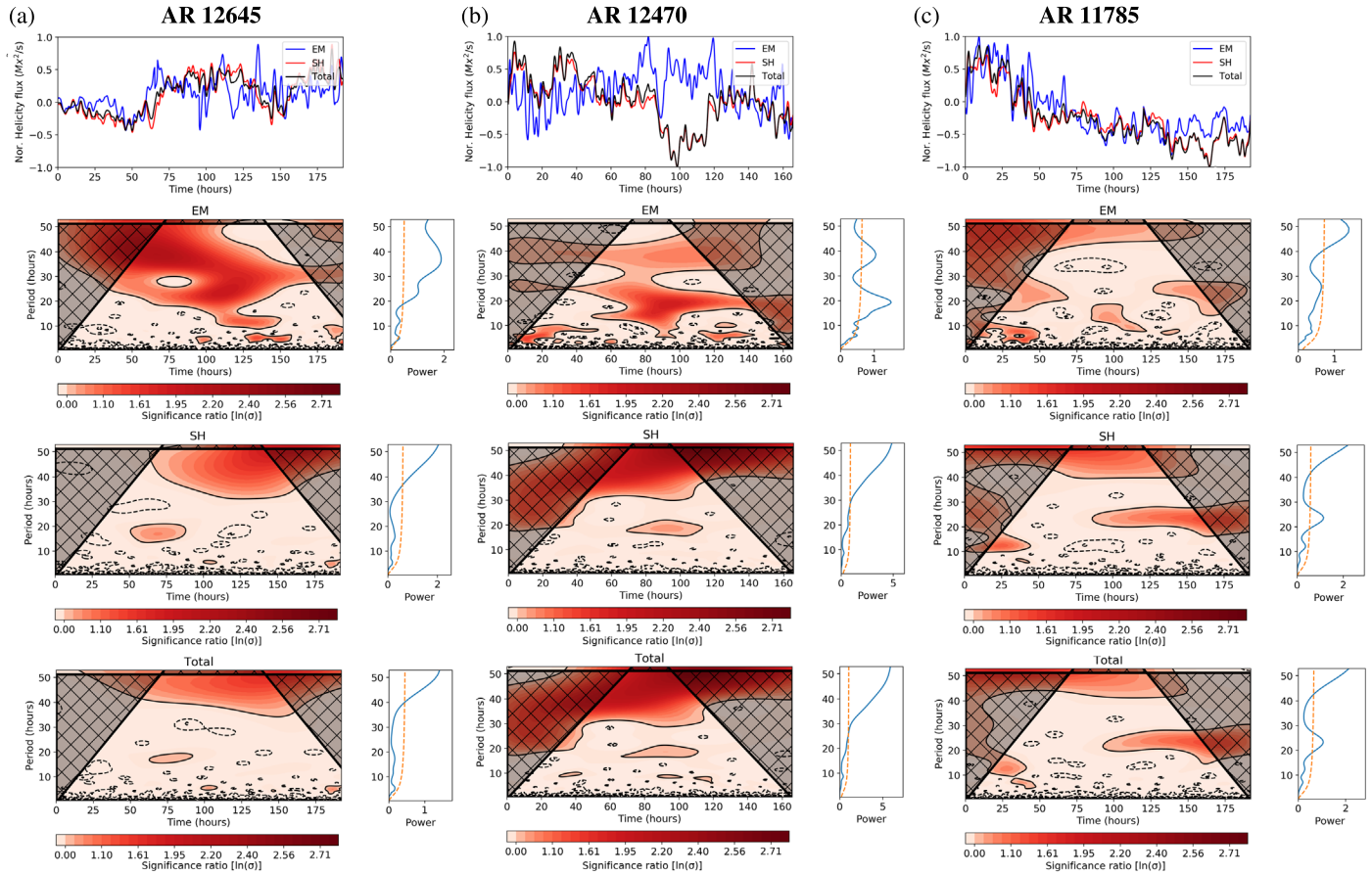

Figure 3. Same as Figure 2, but for the three non-flaring ARs, namely (a) AR 12645, (b) AR 12470, and (c) AR 11785.

sporadically present in the EM and SH time series. However, this peak appears only after the X1.6 flare in the evolution of the total flux data. The lifetime of the ∼35 hr periodicity is longer than five cycles in the case of the three helicity flux components. Nevertheless, the ∼10 hr period is observed through 20 cycles in the case of the EM, while this periodicity is continued during 13/11 cycles in the SH/total data.

3. AR 11890: similar to AR 12192, we identify common peaks at two distinct periodicities in the three helicity components prior to the X-class flares in Figure 2(c). The first peak period is ∼8 hr, which appears before the X3.3 and the first X1.1 flare, respectively. This ∼8 hr period decays after 10 cycles, just after the first X1.1 event. In the case of the second X1.1 flare, the ∼28 hr periodicity peak becomes a common feature only from ∼115 hrs in the WPS of the EM, SH, and total flux components. The ∼28 hr peak appears earlier and is observable throughout five cycles in the EM, compared to a lifetime of only three cycles in the SH and total flux components.

Common significant periodicities are absent in the helicity flux components of the three non-flaring AR. Only the EM flux time series of ARs 12470 and 12645 show some peaks in the WPS and GPS of Figure 3. In the case of AR 12645, there are periods of 5/23/37 hr over 18/6/5 cycles, respectively. AR 12470 also shows ∼7/9/19/39 hr periods, which are observed through 23/18/9/4 cycles in the evolution of the EM flux, respectively. In the case of AR 11785, the SH and the total has a 23 hr period with three cycles only.

From Figures 2–3 we conclude that shorter periods (5–10 hr) mostly appear when an AR is in the fully developed phase (e.g., ARs 12192 and 12470). At this stage, small amounts of flux appear or disappear but the total flux of an AR does not change dramatically. AR 11890 has shorter periods until the magnetic fluxes start to break apart and slowly dissipate. In the case of AR 12645, the 5 hr period becomes significant as the AR reached its fully developed phase. It seems that long-term periodicities are present during the entire lifetime of an AR.

The WPS and GPS of the non-flaring ARs reveal no evidence for the 24 or 12 hr oscillations that are claimed to be present in HMI data due to the orbital motion of the SDO spacecraft. This effect has been reported by Liu et al. (2012), where the Zeeman splitting coupled with the Doppler effect due to the Sun's rotation and the spacecraft motion causes the spectral line to shift every 12 and 24 hr. Smirnova et al. (2013a, 2013b) found that the amplitude of these oscillations increases rapidly when the field strength exceeds 2000 G in the magnetic fields of ARs. Kutsenko & Abramenko (2016) further argued for the presence of these two artificial oscillations by studying wavelet transform of the solar mean magnetic field measurements. If these oscillations were indeed significant in the helicity components presented in this work, we would expect to see them in the WPS of all ARs, particularly in the non-flaring regions where there are very few periodicities of significant power. If they are present, they are weak, and below the threshold significant levels.

4. Summary and Discussion

Comparing the evolution of the helicity fluxes between the flaring and non-flaring ARs is important, as it reflects the dynamic evolution of an AR. The magnetic helicity is uniquely related to the geometrical complexity of the underlying magnetic system, determined by the twist and writhe of individual magnetic field lines, as well as their mutual entanglement. Therefore, the helicity plays an important role in solar activity phenomena, and, the magnetic-helicity-based quantities may be efficient for the purpose of flare prediction (see, e.g., Pariat et al. 2017; Thalmann et al. 2019, and references therein). It remains a challenging task to find an improved characterization of the evolution of helicity injection inside an AR, and employ this information as a practical tool in the context of flare prediction.

In this work, we determine the emergence, shearing, and total helicity components of six ARs by using the DAVE4VM algorithm (Schuck 2008). Three ARs produced intensive solar flare eruptions and another three ARs were host of smaller B- and C-class flares only. In the case of flaring/non-flaring groups, one AR was selected to represent each of the three morphology phases of formation, fully developed, and decay. Following a wavelet analysis of the time series of normalized helicity flux components, we found the following.

1. Flaring ARs show common and rather powerful periodicities in the time series of the normalized emergence, shearing, and total helicity fluxes. These common periodicities tend to appear before the occurrence of the large flares.
2. Non-flaring ARs do not possess such clear common periodicities present in the three magnetic helicity components.
3. Shorter periods, e.g., between 5 and 10 hr, are observable when an AR is in its fully developed evolutionary phase.
4. Longer periods are present during an AR's lifetime. The identified longer periods are found to be comparable with the results of Goldvarg et al. (2005). They found a 48 hr periodicity of the energy release of ARs in a larger statistical example.

The periodicity of EM and SH components of magnetic helicity may reflect the evolution of ARs where the magnetic flux emergence, the complexity evolution, and the subsequent energy release, do not occur monotonically but by alternating and periodic phases. Supporting Pariat et al. (2017) and Thalmann et al. (2019), we can also conclude that the three helicity flux components are together capable to reveal the threat of a flaring AR, but not the magnitude of an upcoming eruption. Our findings demand a similar analysis on a much larger data set to draw more firm conclusions about the flaring precursor capability and accuracy of helicity flux.

The authors are grateful to an anonymous referee for constructive comments and recommendations that helped to improve the readability and quality of this Letter. M.B.K. and H.M. are grateful to the Science and Technology Facilities Council (STFC; UK, Aberystwyth University, grant No. ST/S000518/1), for the support received while conducting this research. All authors acknowledge the SOLARNET Mobility Programme grant No. 824135. R.E. is grateful to STFC (UK, grant No. ST/M000826/1) and EU H2020 (SOLARNET, grant No. 158538). R.E. also acknowledges support from the Chinese Academy of Sciences President's International Fellowship Initiative (PIFI; grant No. 2019VMA0052) and The Royal Society (grant No. IE161153). P.R. acknowledges support by the Italian MIUR-PRIN grant 2017APKP7T on Circumterrestrial Environment: Impact of Sun–Earth Interaction. The research leading to these results has received funding from the European Union's Horizon 2020 research and innovation program under grant agreement No. 739500 (PRE-EST project) and No. 824135 (SOLARNET project). This work was supported by the Italian MIUR-PRIN 2017 on Space Weather: impact on circumterrestrial environment of solar activity, by Space Weather Italian COmmunity (SWICO) Research Program, and by the Università degli Studi di Catania (Piano per la Ricerca Università di Catania 2016–2018—Linea di intervento 1 "Chance"; Linea di intervento 2 "Ricerca di Ateneo—Piano per la Ricerca 2016/2018"; "Fondi di ateneo 2020–2022, Università di Catania, linea Open Access").

ORCID iDs

M. B. Korsós https://orcid.org/0000-0002-0049-4798
P. Romano https://orcid.org/0000-0001-7066-6674
H. Morgan https://orcid.org/0000-0002-6547-5838
Y. Ye https://orcid.org/0000-0002-1854-8459
R. Erdélyi https://orcid.org/0000-0003-3439-4127
F. Zuccarello https://orcid.org/0000-0003-1853-2550

References

Adams, J. C. 1993, Appl. Math. Comput., 53, 235
Barnes, G., Leka, K. D., Schrijver, C. J., et al. 2016, ApJ, 829, 89
Berger, M. A. 2003, in Advances in Nonlinear Dynamos, ed. A. Ferriz-Mas & M. Núñez (London: CRC Press), 345
Berger, M. A. 1984, GApFD, 30, 79
Berger, M. A. 1997, JGR, 102, 2637
Berger, M. A., & Field, G. B. 1984, JFM, 147, 133
Berger, M. A., & Ruzmaikin, A. 2000, JGR, 105, 10481
Bobra, M. G., Sun, X., Hoeksema, J. T., et al. 2014, SoPh, 289, 3549
Campi, C., Benvenuto, F., Massone, A. M., et al. 2019, ApJ, 883, 150
Démoulin, P., Mandrini, C. H., van Driel-Gesztelyi, L., et al. 2002, A&A, 382, 650
Eastwood, J. P., Biffis, E., Hapgood, M. A., et al. 2017, RiskA, 37, 206
Elmhamdi, A., Romano, P., Kordi, A. S., & Al-trabulsy, H. A. 2014, SoPh, 289, 2957
Elsasser, W. M. 1956, AmJPh, 24, 85
Florios, K., Kontogiannis, I., Park, S.-H., et al. 2018, SoPh, 293, 28
Gao, Y. 2018, RAA, 18, 028
Georgoulis, M. K., Nindos, A., & Zhang, H. 2019, RSPTA, 377, 20180094
Goldvarg, T. B., Nagovitsyn, Y. A., & Solov'Ev, A. A. 2005, AstL, 31, 414
Hale, G. E., & Nicholson, S. B. 1925, CMWCI, 300, 1
Korsós, M. B., Yang, S., & Erdélyi, R. 2019, JSWSC, 9, A6
Kusano, K., Maeshiro, T., Yokoyama, T., & Sakurai, T. 2004, in ASP Conf. Ser. 325, Study of Magnetic Helicity in the Solar Corona, ed. T. Sakurai & T. Sekii (San Francisco, CA: ASP), 175
Kutsenko, A. S., & Abramenko, V. I. 2016, SoPh, 291, 1613
Leka, K. D., Park, S.-H., Kusano, K., et al. 2019, ApJS, 243, 36
Linton, M. G., Dahlburg, R. B., & Antiochos, S. K. 2001, ApJ, 553, 905
Liu, Y., Kurokawa, H., Liu, C., et al. 2007, SoPh, 240, 253
Liu, Y., Hoeksema, J. T., Scherrer, P. H., et al. 2012, SoPh, 279, 295
McAteer, R. T. J., Gallagher, P. T., Williams, D. R., et al. 2002, ApJL, 567, L165
Moon, Y. J., Chae, J., Choe, G. S., et al. 2002a, ApJ, 574, 1066
Moon, Y. J., Choe, G. S., Wang, H., et al. 2002b, ApJ, 581, 694
Pariat, E., Leake, J. E., Valori, G., et al. 2017, A&A, 601, A125
Park, S.-H., Cho, K.-S., Bong, S.-C., et al. 2012, ApJ, 750, 48
Park, S.-H., Lee, J., Choe, G. S., et al. 2008, ApJ, 686, 1397
Prior, C., Hawkes, G., & Berger, M. A. 2020, A&A, 635, A95
Chandra, R., Pariat, E., Schmieder, B., Mand rini, C. H., & Uddin, W. 2010, SoPh, 261, 127
Romano, P., Pariat, E., Sicari, M., & Zuccarello, F. 2011, A&A, 525, A13
Romano, P., & Zuccarello, F. 2011, A&A, 535, A1

Schuck, P. W. 2008, ApJ, 683, 1134
Smirnova, V., Efremov, V. I., Parfinenko, L. D., Riehokainen, A., & Solov'ev, A. A. 2013a, A&A, 554, A121
Smirnova, V., Riehokainen, A., Solov'ev, A., et al. 2013b, A&A, 552, A23
Smyrli, A., Zuccarello, F., Romano, P., et al. 2010, A&A, 521, A56
Taylor, J. B. 1974, PhRvL, 33, 1139
Thalmann, J. K., Moraitis, K., Linan, L., et al. 2019, ApJ, 887, 64
Toriumi, S., & Wang, H. 2019, LRSP, 16, 3
Torrence, C., & Compo, G. P. 1998, BAMS, 79, 61
Tziotziou, K., Georgoulis, M. K., & Liu, Y. 2013, ApJ, 772, 115
Vemareddy, P., Ambastha, A., Maurya, R. A., & Chae, J. 2012, ApJ, 761, 86
Wang, S., Liu, C., Deng, N., & Wang, H. 2014, ApJL, 782, L31
Wang, Y., Liu, J., Jiang, Y., & Erdélyi, R. 2019, ApJ, 881, 15
Woltjer, L. 1958, ApJ, 128, 384